Microflow of nanoemulsion threads in surfactant solutions

Thai Dinh,[1] Yixuan Xu,[2] Thomas G. Mason,[3,4] and Thomas Cubaud[1,*]

[1]*Department of Mechanical Engineering, Stony Brook University, Stony Brook, New York 11794, USA*
[2]*Department of Materials Science and Engineering, University of California–Los Angeles, Los Angeles, California 90095, USA*
[3]*Department of Chemistry and Biochemistry, University of California–Los Angeles, Los Angeles, California 90095, USA*
[4]*Department of Physics and Astronomy, University of California–Los Angeles, Los Angeles, California 90095, USA*

(Received 28 August 2022; accepted 14 December 2022; published 6 January 2023)

We experimentally investigate the microfluidic flow of oil-in-water nanoemulsions in aqueous sodium dodecyl sulfate (SDS) solutions having different concentrations and injection flow rates. A coaxial microfluidic device is employed to explore the behavior of nanoemulsion threads in these sheathing SDS solutions. Using two high-speed cameras, which simultaneously capture both top and side views, we reveal a variety of flow phenomena, ranging from simple core-annular flow to complex flows, such as gravitational, inertial, and buckling thread flows. By analyzing these complex flows, we develop a methodology that elucidates the relationship of core-annular and gravitational flows at low flow rates. Further, we examine the off-axis displacements and bending of core threads at large flow rates, and we study the buckling dynamics of nanoemulsion threads subjected to osmotic stresses caused by large SDS concentrations in the sheathing fluid.

DOI: 10.1103/PhysRevE.107.015101

I. INTRODUCTION

Nanoemulsions are typically oil-in-water (O/W) or water-in-oil (W/O) emulsions composed of two immiscible fluids and a surfactant emulsifier stabilizer; after emulsification, the average droplet radius is usually in the range between about 5 nm to about 100 nm [1–4]. Most nanoemulsions are produced using either strong ultrasonic excitation (sonication) [5,6] or using high-pressure microfluidic devices (homogenization) [2,7]. Similar to emulsions having larger droplet sizes, nanoemulsions are kinetically stable liquid/liquid dispersions. The small droplet size, however, provides enhanced stability [5] with large surface-to-volume ratios useful for a variety of applications such as pharmaceuticals [8–11], foods [12–16], and cosmetics [17,18]. As a consequence of the wide application of nanoemulsions across many fields, recently, research on nanoemulsions has been focused on formulation aspects that optimize around certain desired compositions, droplet size distributions, and physical properties [3]. However, microfluidic manipulation of nanoemulsions after production has remain largely unexplored to date and the use of rapid real-space visualization methods to study flowing nanoemulsions, which have been previously size-fractionated, would clarify their multiphase transport properties in a dynamic coflowing external solution environment at the small scale.

Microfluidic platforms provide fine control over flow manipulations and microgeometries for multiphase liquid-liquid experiments [19–21] and can be used to explore and visualize intriguing physical processes over a wide range of flow rates [22,23]. Coaxial devices consist of small centerline injectors inserted in microcapillaries and are practical to a range of applications such as synthesis of nanoparticles [24], fabrication of hydrogel structures [25], and flow encapsulation [26]. The possibility to generate monodisperse droplets in microchannels is also useful for synthesizing fine-tune emulsions in porous-like geometries [27,28] and for investigating the role of additives on emulsion stability [29–32]. The sizes of droplets d generated on chip, however, typically scale with the channel dimension h, thereby limiting investigations of emulsions behavior in open microflow systems to a few h/d, i.e., in the slug or segmented multiphase flow regimes. By contrast, for the case of nanoemulsions, the typical number of droplets per channel width can be very large, $h/d \sim 10^4$, which enables experimental access to partially understood regions liquid-liquid multiphase flows in small conduits. Another microflow regime of interest consists of viscous core-annular flows, i.e., coaxial threads coflowing in a less viscous phase due to the independent control of fluid interfacial area and residence time [33]. Such flow configuration is, however, prone to numerous hydrodynamic instabilities, including inertial, diffusive, and buckling destabilization processes [34–36], and less is known about the flow stability of threads made of nanoscale droplets. Hence, microfluidic model studies, which utilize well-characterized colloidal fluids, have the potential to unravel the flow phenomenology of nanodroplets interacting with chemicals at the microscale and to enhance the capabilities of microflow processing techniques.

Here we utilize coaxial microfluidic devices to study the behavior of nanoemulsion in the presence of external flow containing surfactant systematically. We conduct experiments covering different concentrations of the external flowing solution, from diluted to concentrated, varying injection needle sizes, and capturing images from both top and side views of microchannel simultaneously. The basic flow pattern, a core-annular flow, is first investigated at low flow rates to provide

*Corresponding author: thomas.cubaud@stonybrook.edu

 ©2023 American Physical Society

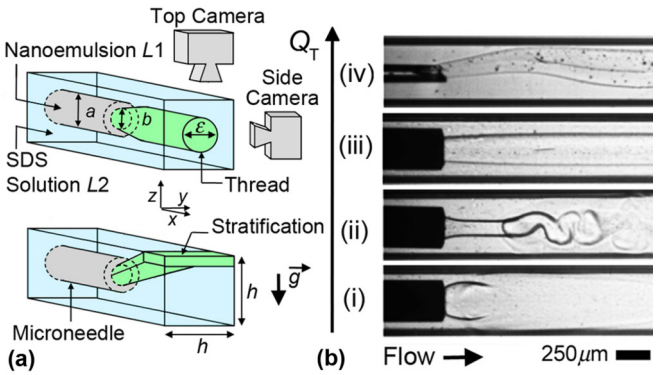

FIG. 1. (a) Schematics of the coaxial microfluidic contactor having an internal cylindrical microcapillary needle (gray) and an optically transparent external square glass microcapillary of width h. Upper schematic: the centrally injected nanoemulsion thread ($L1$, green) expands to a steady-state diameter ε downstream surrounded by surfactant solution ($L2$, light blue); top and side cameras simultaneously image this process. Lower schematic: for oil-in-water nanoemulsions containing an oil that is less dense than water, gravitational forces can cause stratification of the nanoemulsion thread against the upper wall downstream. (b) Examples of observed thread flow regimes for increasing total volumetric flow rates, Q_T: (i) gravitational, (ii) buckling, (iii) stable, and (iv) inertial (top view).

a foundation for analysis of more complex flows observed at extreme flow rates. We then analyze the lower extreme in which central stream of nanoemulsion is affected by gravity and buoyantly lifted to the enclosing upper wall. In addition, we study buckling instabilities at large surfactant concentration, and we examine displacements of central nanoemulsion threads from the centerline of the microchannel at high flow rates. We both quantitatively and qualitatively analyze characteristics of nanoemulsion flows over a wide range of flow rates and parameters.

II. EXPERIMENTAL METHODS

We employ coaxial microchannels to investigate the flow behavior of O/W nanoemulsion threads, which have a fixed nanodroplet volume fraction and surfactant concentration prior to injection, coflowing in a sheathing surfactant solution at various surfactant concentrations C_2. The microchannel consists of a square capillary having an internal width $h = 500\,\mu$m and a circular inner microneedle having outer diameter a and inner diameter b [Fig. 1(a)]. To examine the role of geometry, we use three microneedles having $b/h = 0.10$ and $b/a = 0.50$ for the "small" needle, $b/h = 0.30$ and $b/a = 0.50$ for the "medium" needle, and $b/h = 0.51$ and $b/a = 0.56$ for the "large" needle. The small microneedle is fabricated using a micropipette puller, thereby creating long tapered needles with parallel walls, which are sometimes referred to as aspiration pipettes. The medium and large microneedles are stainless steel dispensing needles that have blunt flat tips. The circular capillary is inserted to the square capillary using a guiding system for initial alignment. Two high-speed cameras are positioned on top and on the side of the microfluidic platform; these simultaneously record 3D flow morphologies for subsequent image analysis. This two-camera setup visualization technique also allows us to position the inner microneedle along the centerline of the square capillary precisely using a micro-stage attached to the outlet of the coaxial microchannel.

TABLE I. Physical properties of fluid pairs, labeled A, B, and C, according to different SDS concentrations C_2: dynamic viscosity η_2, mass density ρ_2, and dimensionless density difference $\Delta\rho/\rho_1$.

Fluid Pair	C_2 (mM)	η_2 (cP)	ρ_2 (g/ml)	$\Delta\rho/\rho_1$
A	10	1.03	1.003	0.012
B	100	1.11	1.029	0.038
C	200	1.29	1.057	0.066

Polydisperse O/W nanoemulsions, composed of conventional silicone oil (poly-dimethylsiloxane, PDMS) having kinematic viscosity $\nu_O = 10$ cSt and an aqueous solution of sodium dodecyl sulfate (SDS), are first produced using multiple passes in a microfluidic homogenizer (Microfluidizer) [2]. This polydisperse nanoemulsion is then subjected to a series of ultracentrifugal size-fractionation steps, yielding a master uniform nanoemulsion having an initial oil volume fraction $\Phi_i = 0.496$ and average droplet radius $\langle a_d \rangle = 46$ nm. The polydispersity, proportional to the width of the monomodal peaked droplet size distribution, as determined by dynamic light scattering, is $\delta a_d/\langle a_d \rangle \approx 0.25$. This multistep ultracentrifugation process is simultaneously used to set the SDS concentration in the aqueous continuous phase of the nanoemulsion to $C_1 = 10$ mM, just above the critical micelle concentration of $C^* \approx 8$ mM for SDS [37]. This master nanoemulsion is subsequently diluted down to a final droplet volume fraction $\Phi_f = 0.17$ using a 10 mM aqueous solution of SDS. This dilution provides a viscous dispersion, well below the nanodroplet jamming point for this $\langle a_d \rangle$, amenable for controlled microfluidic injections. The viscosity of the final nanoemulsion is measured using a miniature falling ball viscometer [38], and we find a dynamic viscosity of $\eta_1 = 18.15$ cP. The final nanoemulsion's mass density is $\rho_1 = 0.991$ g/ml. During the microflow experiment, the final nanoemulsion fluid $L1$ is introduced in the microneedle at a volumetric flow rate Q_1 and the external phase $L2$ is injected at volumetric flow rate Q_2 in the square capillary using two separately controlled syringe pumps [Fig. 1(a)] connected to the coaxial devices with microfluidic connectors. We examine and report the multiphase flow behavior for three SDS concentrations C_2 in $L2$: 10, 100, and 200 mM. Hence, three fluid pairs, whose properties are shown in Table I, are systematically investigated. For fluid pairs B and C, the SDS concentrations C_2 are far in excess of C^*; so, there are substantial concentrations of SDS micelles in $L2$. Furthermore, as fluids $L1$ and $L2$ are both above C^*, the interfacial tension γ_{12} between oil and SDS solutions is expected to remain constant with negligible Marangoni stresses and, as the continuous phase of $L1$ is fully miscible with $L2$, no effective interfacial tension is assumed between adjacent streams.

The interplay between fluid properties, such as fluid viscosities η_1 and η_2, densities ρ_1 and ρ_2, and surfactant concentration C_2, together with flow parameters, including the

volumetric flow rates Q_1 and Q_2 of $L1$ and $L2$ respectively, leads to several different flow regimes. In particular, a large viscosity contrast $\chi = \eta_1/\eta_2 \sim 10^1$ between the central fluid $L1$ and the external sheathing fluid $L2$ in compact geometries facilitates the formation of viscous threads [39], which are prone to various hydrodynamic instabilities [40]. Figure 1(b) provides examples of the four main types of flow regimes observed in this work as a function of the total volumetric flow rate $Q_T = Q_1 + Q_2$. At very low Q_T, the small, yet nonnegligible, density difference $\Delta\rho$ between $L1$ and $L2$ yields (i) a gravitational regime, where the buoyant thread progressively drifts upward, contacts the top channel wall, and creates a viscous layer as seen from top view, and at low Q_T, (ii) a buckling regime is observed for large external phase surfactant concentration C_2. At moderate Q_T, the central stream forms a straight thread near the fluid contactor region in (iii) the viscous regime. When the total flow rate Q_T is very large, the central stream bends after exiting the microneedle tip and deviates from the center of the channel in (iv) the inertial regime. In this following, we systematically examine thread dynamics for each fluid pair and microgeometry over a wide range of flow rates. This method enables quantitative comparisons to be made and reveals the roles of fluid properties and flow parameters on thread stability, thereby providing insights into the complex microflow behavior of multicomponent materials.

III. CORE-ANNULAR FLOWS

We first turn our attention to the features of regular flow regimes, such as the characteristics of stable threads, which provide a basis for later characterization of irregular flow patterns. The simple core-annular flow configuration consists of a straight central stream of $L1$ with diameter ε, which is sheathed and convected by side stream $L2$ along the parallel channel [Fig. 2(a)]. In our experiment, this flow pattern is observed with all fluid pairs and needle sizes. To determine the impact of the needle size b and flow rate ratio φ on thread formation, we analyze the evolution of ε/h along channel length x/h, where $x = 0$ corresponds to the needle tip, using image-processing techniques [Fig. 2(b)]. As can be seen, the thread diameter ε reaches a nearly constant value ε_0 at relatively short distance from the contactor $x/h \sim 2$. Incidentally, the sudden increase or decrease of ε from the initial b at $x = 0$ leads to a local deceleration or acceleration of the nanoemulsion, which does not significantly alter thread behavior in the viscous regime at moderate Q_T. In the case of circular capillaries, an analytical solution of the Navier-Stokes equations for two miscible fluids leads to a simple relationship between stable thread diameter ε_0 and flow rate ratio $\varphi = Q_1/Q_2$ at large $\chi \gg 1$, according to $\varepsilon_0/h = [\varphi/(\varphi+2)]^{1/2}$ in the absence of diffusion phenomena [40]. This equation shows that ε_0 is essentially controlled by the flow rate ratio $\varphi = Q_1/Q_2$. To probe the role of flow velocity on stable thread diameter, we measure the evolution ε_0 as a function of Q_T for fixed values of φ, from small to large thread size [Fig. 2(c)]. Data show that the stable diameter remains independent of flow velocity in the viscous regime. Therefore, we plot the average thread diameter ε_0 as a function of flow rate ratio φ and find excellent agreement with theory, with data collapsing

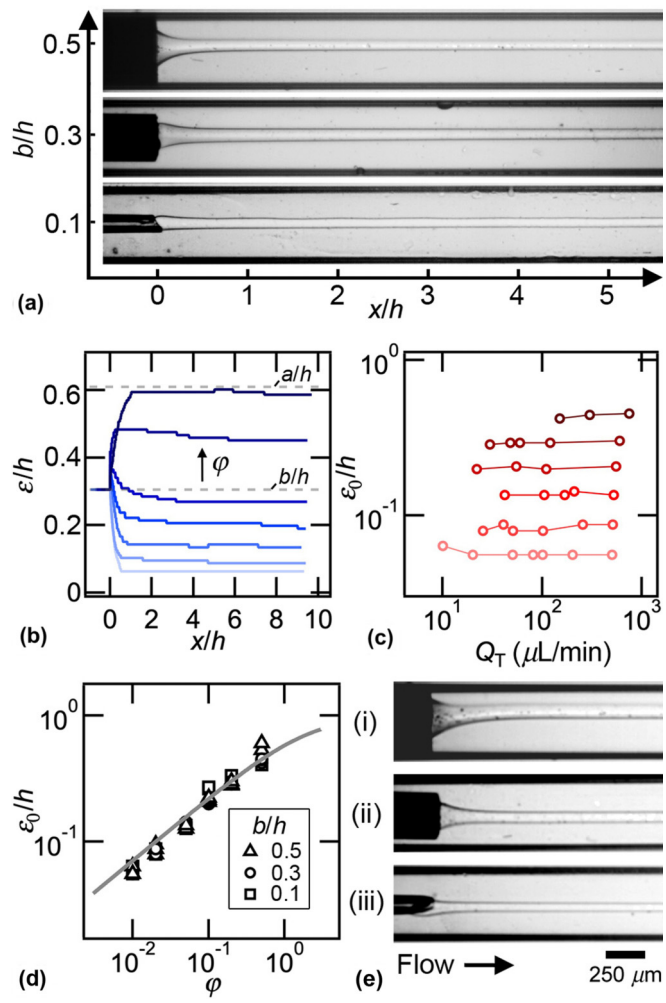

FIG. 2. Stable thread regime. (a) Top view micrographs of regular threads in various needles at identical flow rates, $Q_1 = 1$ and $Q_2 = 20\,\mu$l/min, fluid pair A. (b) Evolution of central stream diameter ε/h along channel length x/h, fluid pair A, $C_2 = 10$ mM, medium needle size. (c) Evolution of stable thread diameter ε_0/h as a function of total flow rate Q_T at various fixed φ, fluid pair B, $C_2 = 100$ mM, middle needle size. (d) Relationship between ε_0/h and flow rate ratio φ for fluid pair B in various microdevices, solid line: $\varepsilon_0/h = [\varphi/(\varphi+2)]^{1/2}$. (e) Top view micrographs of slightly eccentric stable threads in diverse microgeometries.

onto the predicted master curve, for these three fluid pair and needle configurations [Fig. 2(d)]. While the thread diameter follows a simple scaling equation, in practice, the deviation of thread alignment with the centerline y_0 remains small compared to the apparent microneedle alignment [Fig. 2(e)]. Previous work, investigating the relationship between thread eccentricity y_0 and diameter ε_0 with Newtonian fluids [41], has shown that ε_0 remains constant for $|y_0/h| < 0.3$ due to the parabolic flow of the ensheathing external phase. Therefore, using stable thread diameter of core-annular flow as reference enables identification of other regimes, such as unstable core-annular flow at large flow rates in the inertial regime.

The sudden change in flow geometry at the needle tip of a coaxial microchannel is prone to hydrodynamic instabilities due to the joining of shear layers with varying boundary con-

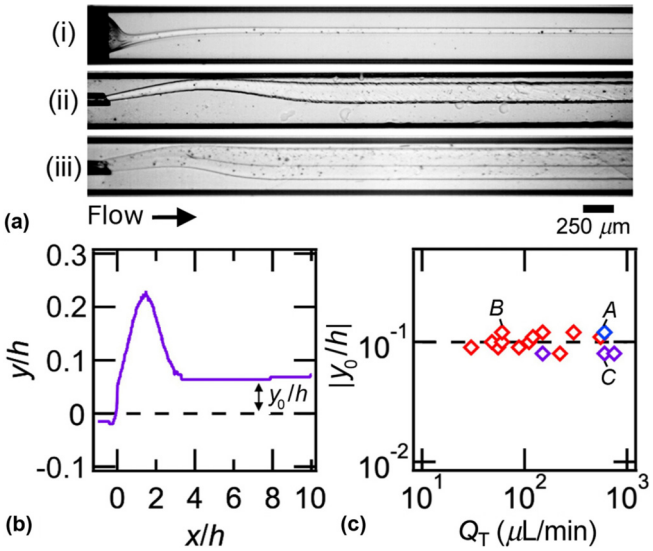

FIG. 3. Inertial thread regime. (a) Top view micrographs of bended threads, (Q_1, Q_2) in μl/min, (i) (10, 500), fluid pair B, large needle, (ii) (250, 500), fluid pair A, small needle, (iii) (250, 500), fluid pair C, small needle. (b) Spatial evolution of thread alignment with centerline y along channel direction x/h for case (a)(iii). (c) Measurement of relative thread eccentricity $|y_0/h|$ as a function of total flow rate Q_T.

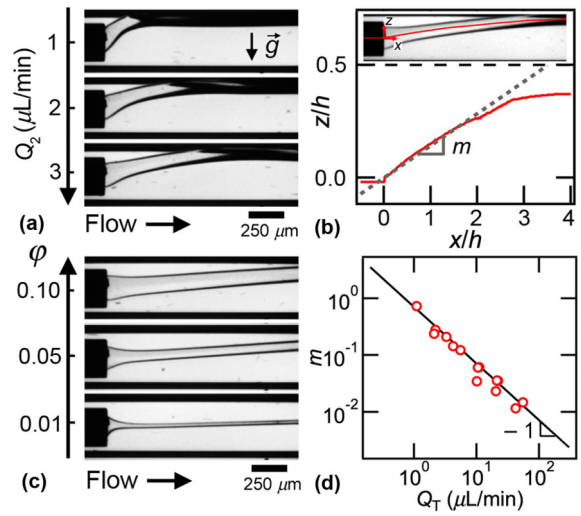

FIG. 4. Side view of gravitational thread regime. (a) Micrographs of inclined threads for fixed $\varphi = 0.1$, fluid pair B, medium needle. (b) Centerline shape of central stream $\varphi = 0.1$, $Q_2 = 5\,\mu$l/min, dash line: linear fit of initial shape showing measurement of slope m. (c) Micrographs of inclined threads at various φ for fixed $Q_2 = 10\,\mu$l/min, fluid pair B, $b/h = 0.3$. (d) Evolution of slope m as a function of total flow rate Q_T for fluid B, Solid line: $m = 0.71\,Q_T^{-1}$.

ditions. In addition, for small inner-to-outer needle diameter b/a, recirculating zones of external fluid are expected to form at moderate Reynolds numbers and perturb regular thread formation. Here the presence of an inertial instability near the needle tip is observed at large Q_T with the formation of locally bended threads [Fig. 3(a)]. In this regime, center thread diameter ε/h gradually increases as the thread is convected downstream and the thread eccentricity y reaches a peak near $x/h \sim 2$ [Fig. 3(b)]. Overall one finds that beside a strong initial deformation near the tip, the thread adopts a straight shape further downstream with slight eccentricity $|y_0/h| \sim 10^{-1}$ [Fig. 3(c)]. While this regime presents features of interest in the context of hydrodynamic instabilities at large microflow velocities, the role of fluid properties appears less pronounced in the case of the inertial regime, and we focus in the remainder of this study on flow patterns formed at relatively low velocities.

IV. GRAVITATIONAL THREAD REGIME

Multicomponent flows at small scales are typically dominated by surface forces, including surface tension and viscous drag; however, differences in fluid densities can still lead to gravitational effects. Here our study reveals that nanoemulsion threads, coflowing in a sheath of their own continuous phase at various surfactant concentrations, are in fact buoyant as a consequence of the lower mass density of the PDMS silicone oil. Examples of drifting threads at low flow velocities are captured using the side camera and shown in Fig. 4(a). Differences in density $\Delta\rho$ between central and side streams drive the core thread upward by buoyancy, and threads are seen to contact the top wall of channel near the fluid junction at low flow rates. To quantify such combination of free vertical convection, due to differing densities and forced horizontal convection caused by imposed injection flow rates and channel geometry, we examine the spatial evolution of the thread centerline along the flow direction [Fig. 4(b)]. The x-z centerline coordinates of threads are determined from side-view micrographs using image processing to extract z coordinates of top and bottom boundaries, which are averaged for a given x to obtain the centerline position. Data show that upon discharge from the microneedle, threads adopt a linear and inclined trajectory that progressively flattens near the top wall further downstream. This method enables us to measure the initial slope of the centerline m to further characterize this regime. As can be seen in Fig. 4(c) for a set of threads formed at fixed Q_T but various φ, the inclination angle remains relatively independent of thread size.

These observations of morphologies of buoyant threads in microchannels contrast with previous studies of liquid jet flows discharging horizontally, a situation commonly encountered with jets entering large, stagnant pools [42]. In these prior studies, a parabolic trajectory is obtained through conservation of momentum. In our situation, however, viscous drag dominates pressure drag, resulting in a linearly inclined trajectory, the orientation of which is set by the upward drift velocity w and the horizontal velocity u driven by forced flow rates in the microchannel. Free convection problems are often treated using the Boussinesq approximation, i.e., neglecting variations of the density except in the gravitational force [43]. Here this approach leads to a scaling of the form $w \sim \Delta\rho g h^2/\eta$ for the vertical Stokes velocity of the thread and the horizontal velocity follows a simple relationship $u \sim Q_T/h^2$. Hence, the slope $m = dz/dx = w/u$ is expected to scale inversely proportional to the flow velocity $m \sim Q_T^{-1}$. This prediction is confirmed experimentally, as shown in Fig. 4(d), where the measurements are well-fit with

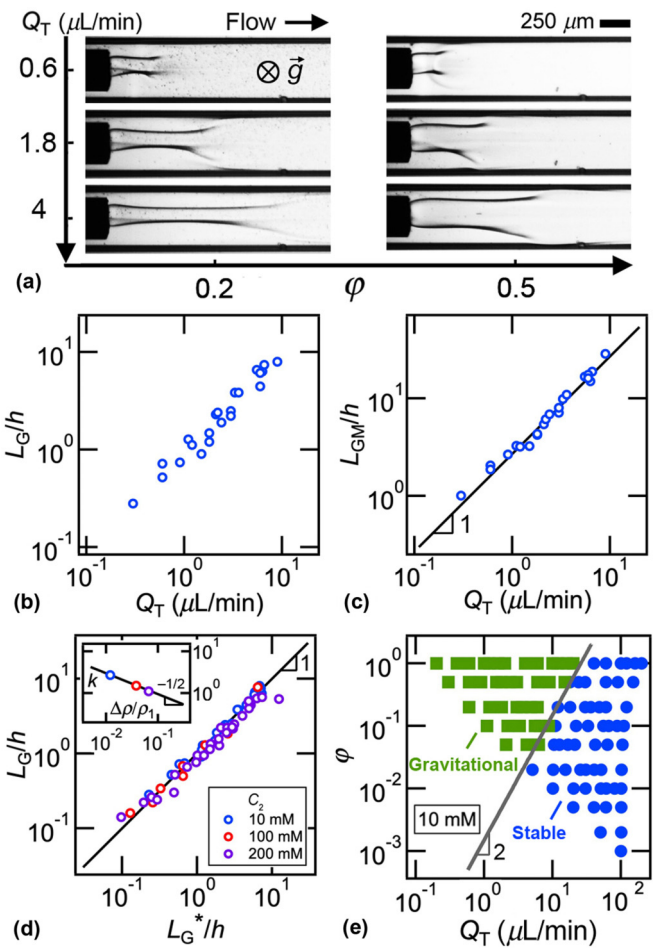

FIG. 5. Top view of gravitational thread regime. (a) Micrographs of gravitational threads, Fluid pair A, medium needle. (b) Direct measurement of L_G/h vs Q_T for fluid pair A, middle needle. (c) Evolution of modified gravitational length L_{GM}/h as a function of Q_T, for fluid pair A, middle needle, solid line $L_{GM}/h = 2.7\,Q_T$. (d) Comparison of measured gravitational length L_G/h with length correlation based on slope L_G^*/h, solid line: $L_G/h = L_G^*/h$. Inset: coefficient k as function of $\Delta\rho/\rho_1$, solid line: $k = 0.3(\Delta\rho/\rho_1)^{-1/2}$. (e) Flow map with gravitational and stable thread regime near contactor $x/h \sim 10$, i.e., $L_G/h \leqslant 10$, fluid pair A, medium needle. Solid line: $\varphi = 1.5 \times 10^{-3} Q_T^2$.

an equation of the form $m = sQ_T^{-1}$, where the coefficient $s = 0.71\ \mu$l/min is expected to depend on the fluid pair, i.e., on fluid densities.

Another important feature of the gravitational regime is the apparent disappearance of the thread as it effectively makes contact with the top wall and spreads out, as seen in the top views displayed in Fig. 5(a). We label the gravitational length L_G as the distance between the needle tip and the thread contact point with the top wall downstream, marking the spatial transition from lubricated threads to gravitationally stratified flows. Direct measurement of L_G/h as a function of Q_T shows significant data scattering [Fig. 5(b)]. Indeed, assuming a straight thread geometry, the gravitational length L_G can be approximated as $L_G = (h/2–\varepsilon/2)/m$, which therefore depends on both thread size ε, i.e., φ, and the slope m, i.e., Q_T and fluid properties. Hence, we introduce the modified gravitational length $L_{GM}/h = 2L_G/(h–\varepsilon)$, which allows for collapsing data onto a single master curve defined as $L_{GM}/h = kQ_T$, where $k = 2.7\ \mu$l/min for fluid pair A [Fig. 5(c)]. We generalize this method to other fluid pairs to determine the dependency of k on fluid densities and experimentally find the scaling $k = 0.3(\Delta\rho/\rho_1)^{-1/2}$ [Fig. 5(d), inset]. Data extracted for top and side views are consistent for fluid pair B given our simplifying assumptions since $s = 0.71$ and $k^{-1} = 0.67\ \mu$l/min. Overall, data suggest the gravitational length can be expressed as $L_G{}^*/h = 0.15(\Delta\rho/\rho_1)^{-1/2}\{1–[\varphi/(\varphi+2)]^{1/2}\}Q_T$. Direct measurements of L_G/h from top view micrographs are in very good agreement with calculated values of L_G^*/h based on flow rates and fluid densities [Fig. 5(d)].

The gravitational length L_G is also a useful parameter to delineate gravitational and stable thread regimes in microfluidic modules having typical flow length in the order of $L_G/h \sim 10^1$. In the case of small threads $\varepsilon/h \ll 1$, the central stream diameter scales as $\varepsilon/h \sim \varphi^{1/2}$, hence a simplified scaling for the transition is found experimentally from flow maps such as $L_G/h \sim Q_T\varphi^{-1/2}$. Indeed, transition curves on (φ, Q_T) phase diagrams are fit with an expression of the form $\varphi \sim Q_T{}^2$ [Fig. 5(e)]. Simple transitions between gravitational and stable regimes are observed for relatively low surfactant concentration of the external phase, such as the one matching that of the nanoemulsion, i.e., $C_2 = 10$ mM. For much higher surfactant concentration C_2, however, substantial applied osmotic stresses are imposed by the sheathing fluid and intriguing buckling instabilities are observed near the transition at low φ, i.e., for small threads.

V. BUCKLING THREAD REGIME

In this section we examine the occurrence of thread buckling instabilities at high surfactant concentrations, i.e., when $C_2 \gg C_1$. Previous work with Newtonian fluids has shown the development of thread folding and coiling behavior in diverging microchannels at large viscosity contrast $\chi \gg 1$ [44,45]. Diverging microgeometries produce locally decelerating flows resulting in lateral stream extension. In the case of highly viscous threads swept away in a low-viscosity phase, however, the thread dilation factor was shown to decrease with χ, resulting in thread bending to conserve mass flow rate. In turn, buckling amplitude and thread deformation increase with viscosity ratio χ. In our current situation, while buckling instabilities are not present for $C_2 = 10$ mM, strong thread destabilization is observed for $C_2 = 100$ and 200 mM in all geometries suggesting an effective increase in χ as a result of surfactant mass transfer from the external phase to the nanoemulsion thread. Likewise, we anticipate that a significant osmotic stress would act to drive water molecules from the continuous phase of the nanoemulsion, which has a much lower SDS concentration, into the external phase resulting in a progressive increase of Φ_f along the thread. Considering the forward water flux out of the thread and the reverse SDS flux into the thread together with steady state convection-diffusion equation using data adapted from [46–48], we estimate the SDS osmotic stress ~0.325 bar and a timescale on the order of 10 ms for the thread to reach a volume fraction of $\Phi_f \sim 0.3$, which is well below the typical thread residence time ~ 1 s in

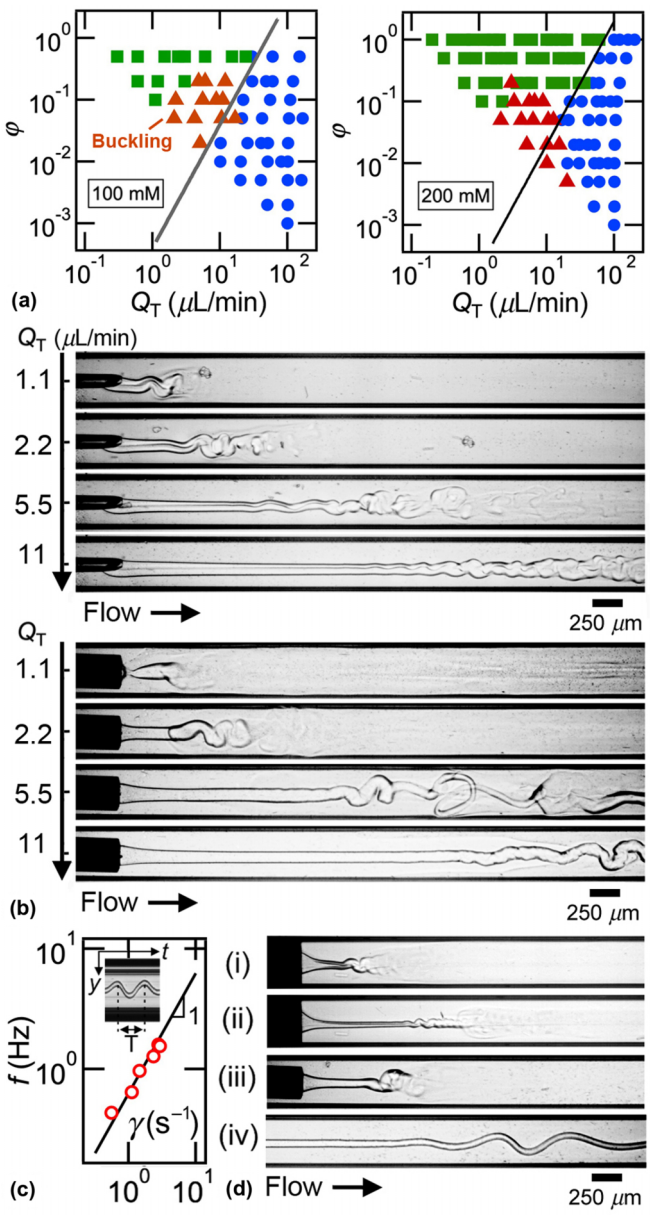

FIG. 6. Buckling thread regime. (a) Flow maps for SDS-rich continuous phase, medium needle. Left: fluid pair B Solid line: $\varphi = 4 \times 10^{-4} Q_T^2$. Right: Fluid pair C, Solid line: $\varphi = 2 \times 10^{-4} Q_T^2$. (b) Top view micrographs of buckling threads with small and medium needles for fixed $\varphi = 0.1$, fluid pair B. (c) Folding frequency f as a function of shear rate γ for fluid B, medium needle. Inset: Spatiotemporal diagram showing measurement of period T. Solid line: $f = 0.62\,\gamma$. (d) Top view micrographs of buckling morphologies, (Q_1, Q_2) in μl/min, (i) (0.1, 0.2), (ii) (0.1, 0.2), fluid pair C, (iii) (0.1, 2), and (iv) (0.5, 10), Fluid pair B.

the field of view at low flow rate Q_T. Fig. 6(a) displays flow maps for these concentrations in the coaxial channels with a middle needle size. Transitions between gravitational and stable thread regimes are well fit with a function of the form $\varphi \sim nQ_T^2$ where the prefactor n increases with the density difference $\Delta\rho$ as expected from previous analysis. For small φ, a buckling region is found in the gravitational regime near the transition to stable threads. Indeed, the thread experiences a significant deceleration upon impinging on the top wall to form slow stratifications. Examples of convective buckling instabilities are shown as a function of Q_T in Fig. 6(b), for fixed flow rate ratio $\varphi = 0.1$ at $C_2 = 100$ mM, and display similar behavior in devices having both small and medium needle sizes. As the contact point of buoyant threads move farther away when the flow velocity increases, strong sinuous deformations develop along the thread further downstream showing the convective nature [49] of this complex solutal instability. Hence, the gravitational regime enables probing thread response to an effective compressive force and the presence of buckling destabilization processes at large C_2 reveals internal thread modification suggesting an increase of effective thread viscosity η_1. We calculate the frequency $f = 1/T$ at which the thread folds using the average time T between two crests of folding, measured from spatiotemporal diagrams, and find a linear relationship with the average shear rate $\gamma = Q_T/h^3$ [Fig. 6(c)]. Overall, a wide range of buckling morphologies are observed; these depend on the fluid compositions and flow rates, including folding and coiling at various aspect ratios [Fig. 6(d)]. While further work would provide additional insights into the buckling behavior of nanoemulsion threads in surfactant-rich environments, our study constitutes an original approach to probe complex physicochemical processes of soft colloidal materials in microgeometries.

VI. CONCLUSIONS

This work has examined the behavior of nanoemulsions coflowing in a sheathing solution containing surfactant. We have first analyzed the stable flow pattern, core-annular flow, and thereby reveal the key dependency of core thread diameter ε on the flow rate ratio φ, and we have discussed the thread bending and displacement y_0 from the centerline at larger velocities. Next, we have reported and explained the impact of gravitationally driven flows at low flow rates. We have shown that our experimental data, specifically the centerline of core thread, deviates from previous work on buoyant jets in an ambient liquid. Herein we have shown that the contact point of a buoyant nanoemulsion jet with a proximate wall in confined environment can be determined using a simple geometrical argument combined with an established relationship between ε and φ. We have subsequently compared our experimental data with calculated data to validate this approach. Finally, we have analyzed the buckling flow regimes for large surfactant concentrations. Future work could explore different external fluids to simulate a particular application environment in which a nanoemulsion would be used. Further theoretical and numerical studies on the unstable folding regime could provide a quantitative understanding of the instability of nanoemulsion threads at low flow rates and at high concentrations of surfactant solutions in the sheathing fluid. This study highlights the interplay of various physical processes on the stability confined viscous jets and clarifies important aspects of microflow manipulations of multicomponent materials having different fluid properties.

[1] K. Meleson, S. Graves, and T. G. Mason, Formation of concentrated nanoemulsions by extreme shear, Soft Mater. **2**, 109 (2004).

[2] T. G. Mason, J. N. Wilking, K. Meleson, C. B. Chang, and S. M. Graves, Nanoemulsions: Formation, structure, and physical properties, J. Phys.: Condens. Matter **18**, R635 (2006).

[3] A. Gupta, H. B. Eral, T. A. Hatton, and P. S. Doyle, Nanoemulsions: Formation, properties and applications, Soft Matter **12**, 2826 (2016).

[4] Y. Singh, J. G. Meher, K. Raval, F. A. Khan, M. Chaurasia, N. K. Jain, and M. K. Chourasia, Nanoemulsion: Concepts, development and applications in drug delivery, J. Control. Release **252**, 28 (2017).

[5] S. Mahdi Jafari, Y. He, and B. Bhandari, Nano-emulsion production by sonication and microfluidization—A comparison, Int. J. Food Prop. **9**, 475 (2006).

[6] T. Delmas, H. Piraux, A. C. Couffin, I. Texier, F. Vinet, P. Poulin, M. E. Cates, and J. Bibette, How to prepare and stabilize very small nanoemulsions, Langmuir **27**, 1683 (2011).

[7] M. J. Hidajat, W. Jo, H. Kim, and J. Noh, Effective droplet size reduction and excellent stability of limonene nanoemulsion formed by high-pressure homogenizer, Colloids Interfaces **4**, 5 (2020).

[8] C.-K. Kim, Y.-J. Cho, and Z.-G. Gao, Preparation and evaluation of biphenyl dimethyl dicarboxylate microemulsions for oral delivery, J. Control. Release **70**, 149 (2001).

[9] D. M. Smith, J. K. Simon, and J. R. Baker, Applications of nanotechnology for immunology, Nat. Rev. Immunol. **13**, 592 (2013).

[10] M. Jaiswal, R. Dudhe, and P. K. Sharma, Nanoemulsion: An advanced mode of drug delivery system, 3 Biotech **5**, 123 (2015).

[11] V. K. Rai, N. Mishra, K. S. Yadav, and N. P. Yadav, Nanoemulsion as pharmaceutical carrier for dermal and transdermal drug delivery: Formulation development, stability issues, basic considerations and applications, J. Control. Release **270**, 203 (2018).

[12] D. J. McClements, E. A. Decker, and J. Weiss, Emulsion-based delivery systems for lipophilic bioactive components, J. Food Sci. **72**, R109 (2007).

[13] C. Qian, E. A. Decker, H. Xiao, and D. J. McClements, Nanoemulsion delivery systems: Influence of carrier oil on beta-carotene bioaccessibility, Food Chem. **135**, 1440 (2012).

[14] K. Bhargava, D. S. Conti, S. R. P. da Rocha, and Y. F. Zhang, Application of an oregano oil nanoemulsion to the control of foodborne bacteria on fresh lettuce, Food Microbiol. **47**, 69 (2015).

[15] F. Donsi and G. Ferrari, Essential oil nanoemulsions as antimicrobial agents in food, J. Biotechnol. **233**, 106 (2016).

[16] L. Pavoni, D. R. Perinelli, G. Bonacucina, M. Cespi, and G. F. Palmieri, An overview of micro- and nanoemulsions as vehicles for essential oils: Formulation, preparation and stability, Nanomaterials **10**, 135 (2020).

[17] M. N. Yukuyama, D. D. M. Ghisleni, T. J. A. Pinton, and N. A. Bou-Chacra, Nanoemulsion: Process selection and application in cosmetics—A review, Int. J. Cosmetic Sci. **38**, 13 (2016).

[18] N. Atrux-Tallau, J. Lasselin, S. H. Han, T. Delmas, and J. Bibette, Quantitative analysis of ligand effects on bioefficacy of nanoemulsion encapsulating depigmenting active, Colloids Surf. B **122**, 390 (2014).

[19] A. S. Utada, A. Fernandez-Nieves, H. A. Stone, and D. A. Weitz, Dripping to Jetting Transitions in Coflowing Liquid Streams, Phys. Rev. Lett. **99**, 094502 (2007).

[20] R. Seemann, M. Brinkmann, T. Pfohl, and S. Herminghaus, Droplet based microfluidics, Rep. Prog. Phys. **75**, 016601 (2011).

[21] S. L. Anna, Droplets and bubbles in microfluidic devices, Annu. Rev. Fluid Mech. **48**, 285 (2016).

[22] O. Bonhomme, A. Morozov, J. Leng, and A. Colin, Elastic instability in stratified core annular flow, Phys. Rev. E **83**, 065301(R) (2011).

[23] T. Dinh and T. Cubaud, Role of interfacial tension on viscous multiphase flows in coaxial microfluidic channels, Langmuir **37**, 7420 (2021).

[24] J. M. Lim, A. Swami, L. M. Gilson, S. Chopra, S. Choi, J. Wu, R. Langer, R. Karnik, and O. C. Farokhzad, Ultra-high throughput synthesis of nanoparticles with homogeneous size distribution using a coaxial turbulent jet mixer, ACS Nano **8**, 6056 (2014).

[25] S. Tottori and S. Takeuchi, Formation of liquid rope coils in a coaxial microfluidic device, RSC Adv. **5**, 33691 (2015).

[26] I. U. Khan, C. A. Serra, N. Anton, and T. Vandamme, Continuous-flow encapsulation of ketoprofen in copolymer microbeads via co-axial microfluidic device: Influence of operating and material parameters on drug carrier properties, Int. J. Pharm. **441**, 809 (2013).

[27] R. K. Shah, H. C. Shum, A. C. Rowat, D. Lee, J. J. Agresti, A. S. Utada, L. Y. Chu, J. W. Kim, A. Fernandez-Nieves, C. J. Martinez *et al.*, Designer emulsions using microfluidics, Mater. Today **11**, 18 (2008).

[28] N. Bremond and J. Bibette, Exploring emulsion science with microfluidics, Soft Matter **8**, 10549 (2012).

[29] T. Krebs, K. Schroen, and R. Boom, A microfluidic method to study demulsification kinetics, Lab Chip **12**, 1060 (2012).

[30] T. Gu, E. W. Q. Yeap, A. Somasundar, R. Chen, T. A. Hatton, and S. A. Khan, Droplet microfluidics with a nanoemulsion continuous phase, Lab Chip **16**, 2694 (2016).

[31] B. Morin, Y. Liu, V. Alvarado, and J. Oakey, A microfluidic flow focusing platform to screen the evolution of crude oil-brine interfacial elasticity, Lab Chip **16**, 3074 (2016).

[32] A. Nowbahar, K. A. Whitaker, A. K. Schmitt, and T.-C. Kuo, Mechanistic study of water droplet coalescence and flocculation in diluted bitumen emulsions with additives using microfluidics, Energy Fuels **31**, 10555 (2017).

[33] T. Cubaud, Swelling of Diffusive Fluid Threads in Microchannels, Phys. Rev. Lett. **125**, 174502 (2020).

[34] T. Cubaud and T. G. Mason, Folding of Viscous Threads in Diverging Microchannels, Phys. Rev. Lett. **96**, 114501 (2006).

[35] T. Cubaud and S. Notaro, Regimes of miscible fluid thread formation in microfluidic focusing sections, Phys. Fluids **26**, 122005 (2014).

[36] J. K. Nunes, H. Constantin, and H. A. Stone, Microfluidic tailoring of the two-dimensional morphology of crimped microfibers, Soft Matter **9**, 4227 (2013).

[37] R. G. Larson, *The Structure and Rheology of Complex Fluids* (Oxford University Press, New York, 1999).

[38] N. Park and T. F. Irvine, The falling needle viscometer a new technique for viscosity measurements, Wärme- und Stoffübertragung **18**, 201 (1984).

[39] T. Cubaud and T. G. Mason, Formation of miscible fluid microstructures by hydrodynamic focusing in plane geometries, Phys. Rev. E **78**, 056308 (2008).

[40] T. Cubaud, B. Conry, X. Hu, and T. Dinh, Diffusive and capillary instabilities of viscous fluid threads in microchannels, Phys. Rev. Fluids **6**, 094202 (2021).

[41] T. Cubaud, D. Henderson, and X. Hu, Separation of highly viscous fluid threads in branching microchannels, Microfluid. Nanofluid. **20**, 55 (2016).

[42] A. Dewan, J. H. Arakeri, and J. Srinivasan, A note on high Schmidt number laminar buoyant jets discharged horizontally, Int. Commun. Heat Mass Transf. **19**, 721 (1992).

[43] D. J. Tritton, *Physical Fluid Dynamics* (Oxford University Press, New York, 1988).

[44] T. Cubaud, B. M. Jose, and S. Darvishi, Folded microthreads: Role of viscosity and interfacial tension, Phys. Fluids **23**, 042002 (2011).

[45] T. Cubaud and T. G. Mason, Interacting viscous instabilities in microfluidic systems, Soft Matter **8**, 10573 (2012).

[46] R. M. Weinheimer, D. Fennell Evans, and E. L. Cussler, Diffusion in surfactant solutions, J. Colloid Interface Sci. **80**, 357 (1981).

[47] A. A. Merdaw, A. O. Sharif, and G. A. W. Derwish, Water permeability in polymeric membranes, Part I, Desalination **260**, 180 (2010).

[48] G. Gadelha, M. S. Nawaz, S. J. Khan, R. Wang, and C. Y. Tang, Assessment of micellar solutions as draw solutions for forward osmosis, Desalination **354**, 97 (2014).

[49] P. Huerre and M. Rossi, in *Hydrodynamics and Nonlinear Instabilities* (Cambridge University Press, Cambridge, 2005).